A Variational Approach to Magnetic Resonance Coil Sensitivity Estimation

Stephen L. Keeling[*] and Roland Bammer[†]

Abstract. A variational method for estimating a magnetic resonance coil sensitivity from its corresponding nonuniform illumination of magnetic resonance images is proposed and analyzed. The estimated sensitivity can then be used to correct nonuniformities and indeed to facilitate high-speed parallel image acquisition. The data available for estimation include two images of the same field of view but obtained with and without a uniform coil sensitivity. The nonuniformly illuminated image is ideally the product of the uniformly illuminated image with the coil sensitivity. Thus, the desired sensitivity is estimated roughly from a quotient of the two given images over the effective data support. However, the measurements are corrupted by noise, the data are discontinuous at tissue boundaries, and yet the coil sensitivity is very smooth. In the selected estimation procedure, the sum of a residual and a high order penalty is minimized. In this form, the problem is related to the surface estimation problem of early vision. In the present context, higher coil sensitivity decay rates are captured non-parametrically by higher order penalties together with natural boundary conditions. The role of alternative penalties and boundary conditions is investigated both analytically and numerically. Although high order operators are often approximated numerically with a product of low order factors, such factorizations are shown here to lead to conspicuously spurious boundary conditions for surface estimation with sparse data support. Furthermore, while finite elements present a natural numerical approach for solving the optimality system, it is demonstrated here that lumping is required to avoid aberrant consequences in the limit of vanishing regularization corresponding to an ever improving signal-to-noise ratio. Finally, with a proper analytical and numerical formulation, the estimation procedure is demonstrated for a magetic resonance imaging application involving parallel image acquisition.

1 Introduction

Radio frequency coils are used in magnetic resonance imaging (MRI) for both nuclear excitation and for signal detection. On the one hand, a large homogeneous coil such as the body coil shown on the left in Fig. 1, may be used for the uniform elucidation of a volume. On the other hand, a smaller surface coil such as those shown on the right in Fig. 1 can be used to resolve local details with greater sensitivity. Surface coils can also be used in parallel to achieve high signal acquisition rates [19]. However, as illustrated in Fig. 2, surface coils suffer from a nonuniform sensitivity in relation to that of a body coil. For a given pair of images, $\mathcal{U}_\mathrm{b}$ and $\mathcal{U}_\mathrm{s}$, measured simultaneously by a body coil and a surface coil, respectively, it is natural to consider using the quotient $\mathcal{Q} = \mathcal{U}_\mathrm{s}/\mathcal{U}_\mathrm{b}$ to correct for the nonuniformity in $\mathcal{U}_\mathrm{s}$ according to $\mathcal{U}_\mathrm{s}/\mathcal{Q}$ [4]. However, $\mathcal{Q}$ becomes practically indeterminate in regions of low signal-to-noise ratio where there is no tissue or low tissue response. Furthermore, for typical applications, this pair of images $(\mathcal{U}_\mathrm{b},\mathcal{U}_\mathrm{s})$ is obtained by a measurement performed specifically for coil sensitivity estimation, and the main investigative measurement requiring the sensitivity is performed subsequently. Because of patient motion between these measurements, the coil sensitivity $\mathcal{C} \approx \mathcal{U}_\mathrm{s}/\mathcal{U}_\mathrm{b}$ is needed in a neighborhood of the zones where a given quotient $\mathcal{Q}$ is initially well-determined, in order to correct for nonuniformities in subsequent measurements. With the data masked to zero in zones of low signal-to-noise, the coil sensitivity estimation must therefore stably interpolate over gaps in and extrapolate outside of the support of the data. Moreover, the measurements are corrupted

---

[*] Institut für Mathematik, Karl-Franzens-Universität Graz, Heinrichstraße 36, 8010 Graz, Austria; email: keeling@uni-graz.at; tel: +43–316–380–5156; fax: +43–316–380–9815. Supported by the Fonds zur Förderung der wissenschaftliche Forschung under SFB 03, “Optimierung und Kontrolle”.

[†] Radiological Sciences Laboratory, R. Lucas MRS/I Center, Department of Radiology, Stanford University, 1201 Welch Road, Stanford, CA 94305-5488, USA; email: roland@s-word.stanford.edu; tel: +1–650–498–4760; fax: +1–650–723–5795. Supported by a grant from the National Institutes of Health (NIH-1R01NS35959).

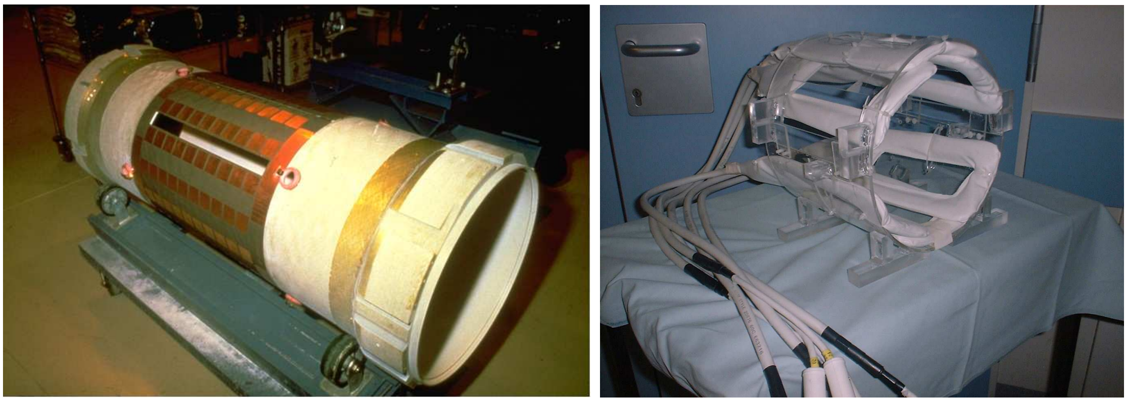

Figure 1: Shown on the left is a magnetic resonance body coil in which a reclining patient may be situated.[‡] Shown on the right are smaller surface coils mounted on a head rack.

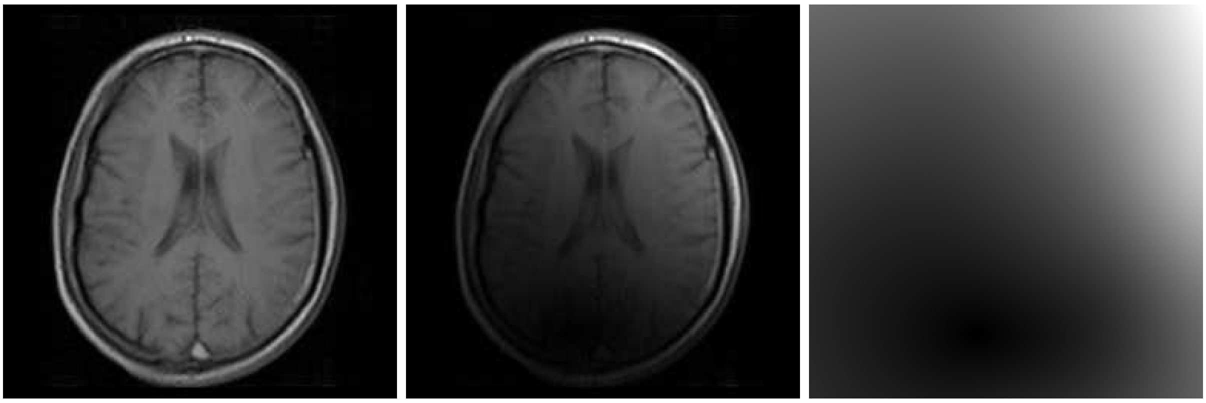

Figure 2: Shown at the left, in the middle, and at the right, respectively, are an image $\mathcal{U}_{\rm b}$ measured with a body coil, an image $\mathcal{U}_{\rm s}$ measured with a surface coil, and an estimated coil sensitivity $\mathcal{C}$.

by noise, the data are discontinuous at tissue boundaries, and yet the coil sensitivity $\mathcal{C}$ is very smooth.

Conventional approaches for this problem have involved filtering techniques employing local polynomials [6] or other basis functions such as thin-plate splines [5] or wavelets [17]. As illustrated in Fig. 3, a typical difficulty with a local estimation procedure is that the variable size of gaps in the support of the data complicates the appropriate choice of local data points to use for interpolation over the gap. Also, while the instability of extrapolation schemes is well known [18], as illustrated in Fig. 3, the problem is exacerbated in lower resolution MRI scans by the typical Gibbs ringing which occurs at the edge of the data support [16]. The use of other basis functions imposes a parameterization on the data and can be unstable unless low dimensional and thereby poor in approximation properties. Of course these parametrized methods can be adapted and regularized for interpolation and extrapolation, and the authors have reported their experience with such methods [6]. However, the non-parametric formulation of the present work has been found to be much more convenient and robust.

In this work, coil sensitivities are determined variationally by minimizing the sum of a residual involving $\mathcal{U}_{\rm b}\mathcal{C} - \mathcal{U}_{\rm s}$ and a regularizing penalty involving derivatives of $\mathcal{C}$. The role of alternative penalties and boundary conditions is investigated in Section 2. Experiments readily reveal the importance of stably representing the estimated sensitivity outside the data support. The extrapolation must also respect the larger sensitivity decay rates associated with smaller radius coils. However, it is proposed here to avoid any explicit solution representation

---

[‡] This image is used with permission from GE Medical Systems.

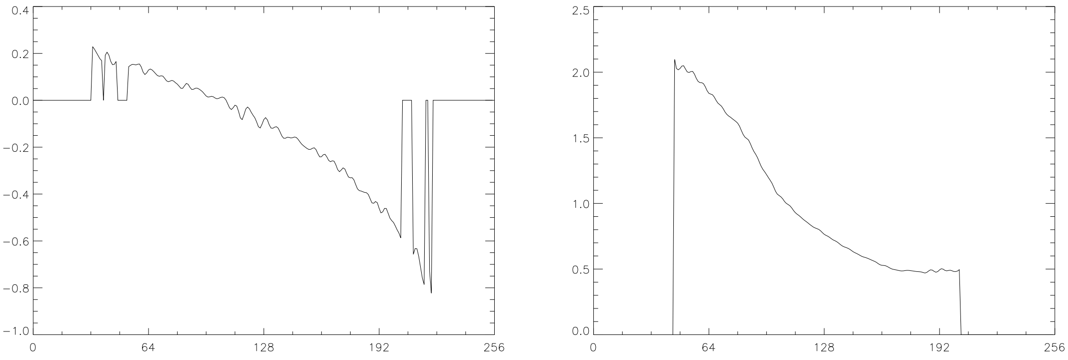

Figure 3: Profiles of typical data showing on the left the variable nature of the data support and on the right the often encountered Gibbs ringing at the edge of the data support.

and to capture higher decay rates implicitly from the local kernel of higher order penalties and their corresponding homogeneous natural boundary conditions. The resulting formulation parallels that of the surface estimation problem of early vision [14]. The relevant analysis of the optimality system, of continuous dependence on data, and of convergence in the limit of diminishing measurement error is summarized in Section 3.

Section 4 begins with a finite difference analysis of the optimality system given in Section 3. Although high order operators are often approximated numerically with a product of low order factors, such factorizations are shown here to lead to conspicuously spurious boundary conditions for surface estimation with sparse data support. Convenient alternatives to factorization are formulated and analyzed, but it is finally proposed to use a finite element discretization investigated in Section 5. While finite elements present a natural numerical approach for solving the optimality system, it is demonstrated here that lumping is required to avoid aberrant consequences in the limit of vanishing regularization corresponding to an ever improving signal-to-noise ratio.

With a proper analytical and numerical formulation, the estimation procedure is demonstrated in Section 6 for a magetic resonance imaging application known as sensitivity encoded (SENSE) image reconstruction [19]. In this application, coils operate in parallel but they undersample the available signal in order to achieve a high acquisition rate. The undersampling leads to an aliased image for each coil, but knowledge of the respective coil sensitivities can be used to reconstruct a single unaliased image. On the other hand, the reconstructed image is susceptible to ghosting artifacts resulting from inaccurate coil sensitivities. These details are demonstrated with magnetic resonance images of phantoms, and the proposed approach is shown to perform quite well for SENSE reconstruction. Finally, the paper concludes in Section 7 with a summary and a description of the forthcoming steps in this research.

2 Variational Formulation

In this section, the variational framework used throughout the paper for coil sensitivity estimation is defined, and the role of alternative penalties and boundary conditions is investigated. For a rectangular image domain $\Omega \in \boldsymbol{R}^N$, let $\mathcal{U}_{\rm s}$ and $\mathcal{U}_{\rm b}$ be images measured with a surface coil and a body coil respectively, and let $\mathcal{C}$ represent the smooth coil sensitivity which is roughly approximated by $\mathcal{U}_{\rm s}/\mathcal{U}_{\rm b}$. Since the raw data obtained by MRI are complex-valued [12], the following manipulations are used for a formulation in terms of real-valued functions:

$$\begin{aligned} |\mathcal{U}_{\rm b}|^2\Re(\mathcal{C}) &\approx \Re(\mathcal{U}_{\rm s})\Re(\mathcal{U}_{\rm b}) + \Im(\mathcal{U}_{\rm s})\Im(\mathcal{U}_{\rm b}) \\ |\mathcal{U}_{\rm b}|^2\Im(\mathcal{C}) &\approx \Im(\mathcal{U}_{\rm s})\Re(\mathcal{U}_{\rm b}) - \Re(\mathcal{U}_{\rm s})\Im(\mathcal{U}_{\rm b}). \end{aligned} \tag{2.1}$$

For a given $\mathcal{U}_\mathrm{b}$ and $\mathcal{U}_\mathrm{s}$, let m represent $|\mathcal{U}_\mathrm{b}|^2$ and let r represent one of the right-hand sides in (2.1). Then for an unknown $\mathcal{C}$, let c represent either $\Re(\mathcal{C})$ or $\Im(\mathcal{C})$ respecting the choice of r. The objective then becomes to estimate c satisfying:

$$mc - r \approx 0. \tag{2.2}$$

Thus, the left-hand side here is the residual to be minimized over a set of smooth functions c.

The final variational formulation adopted in this work is as follows. For $\nu \geq 2$, the coil sensitivity estimation c is the minimizer of the cost:

$$J(c) = \int_\Omega |mc - r|^2 d\boldsymbol{x} + \mu \sum_{|\alpha|=\nu} \frac{\nu!}{\alpha!} \int_\Omega |\partial^\alpha c|^2 d\boldsymbol{x} \tag{2.3}$$

in which the regularization parameter μ controls the trade-off between smoothness and fit-to-data. As shown below, the order of regularization ν controls the estimated coil sensitivity decay rate. Note that the physical decay rate increases accordingly as the radius of a surface coil decreases [12]. Roughly speaking, the penalty of order ν leads to an optimality system of order 2ν in Ω and imposes natural boundary conditions with vanishing derivatives from order ν to $2\nu-1$. As the data are compactly supported in Ω, the solution has vanishing derivatives of order 2ν in a neighborhood of $\partial\Omega$. Since derivatives up to order $\nu - 1$ are free up to the boundary in this neighborhood, the growth or decay supported at the boundary has polynomial degree of at most $\nu - 1$.

For a fuller perspective on (2.3), consider now its alternatives and the experimentation leading to its selection. Instead of the specific form shown in (2.3), suppose only that the cost has the general form:

$$J(c) = \int_\Omega |S(mc - r)|^2 d\boldsymbol{x} + \mu \int_\Omega \phi(|Rc|^2) d\boldsymbol{x} \tag{2.4}$$

and consider the necessary optimality condition [20]:

$$\mu R^* \phi'(|Rc|^2) Rc + mS^*Smc - mS^*Sr = \mu \tilde{R} c + \tilde{S}[c - r/m] = 0 \tag{2.5}$$

where $\tilde{R} = R^*\phi'(|Rc|^2)R$ and $\tilde{S} = mS^*Sm$. Recall that c must be smooth while m and r are rough, and therefore m and r have the same data support Ω_d. Thus, S and $\tilde{S}$ should be smoothing operators or at least not roughen the data, while R and $\tilde{R}$ should be roughing operators or at least not smooth the sensitivity estimate. In contrast to (2.3) assume that $\tilde{R} = I$. Then $\tilde{S}$ should map from functions supported on Ω_d to functions supported on Ω. In other words, $\tilde{S}$ should perform *explicit* interpolation and extrapolation. Such an operator could be constructed as a convolution with a broadly supported kernel which also reflects underlying physics. Similarly, $\tilde{S}$ could be chosen as a projection operator into a span of suitable basis functions. However, these options reflect the conventional approaches mentioned in Section 1, which can be unstable unless low dimensional and thereby poor in approximation properties. Thus, it is proposed here to perform *implicit* interpolation and extrapolation by choosing $S = I$ and selecting the fitting roughing operator.

For instance, suppose first that derivatives of first and second order are penalized to control respectively the influence of data noise on and the accumulation of curvature in the sensitivity estimate:

$$J(c) = \int_\Omega |cm - r|^2 d\boldsymbol{x} + \mu_1 \int_\Omega |\nabla c|^2 d\boldsymbol{x} + \mu_2 \int_\Omega |\Delta c|^2 d\boldsymbol{x}. \tag{2.6}$$

The necessary optimality conditions for the minimization of (2.6) are [20]:

$$\begin{cases} \mu_2 \Delta^2 c - \mu_1 \Delta c + m^2 c = rm, & \Omega \\[2ex] \dfrac{\partial c}{\partial n} = \dfrac{\partial \Delta c}{\partial n} = 0, & \partial\Omega. \end{cases} \tag{2.7}$$

Here, $\partial c/\partial n$ is the normal derivative of c at the boundary $\partial\Omega$ and the conditions at $\partial\Omega$ are the natural boundary conditions. To illustrate the use of this penalty, consider the simple model problem shown in Fig. 4. Let χ_{d} denote the characteristic function for the data support Ω_{d}. In Fig. 4, $m = \chi_{\mathrm{d}}$ and $r = \chi_{\mathrm{d}} c^*$ for a quadratic function c^*. The results shown in Fig. 5 reveal the general trend that the variational estimate behaves very differently in two separate zones, one corresponding to the data support Ω_{d} and the other to the data support complement $\Omega\backslash\Omega_{\mathrm{d}}$. On the other hand, the estimation in Fig. 5 corresponding to $\mu_1 \ll \mu_2$ is much better than that corresponding to $\mu_1 \gg \mu_2$, and suggests that the first order penalty be removed.

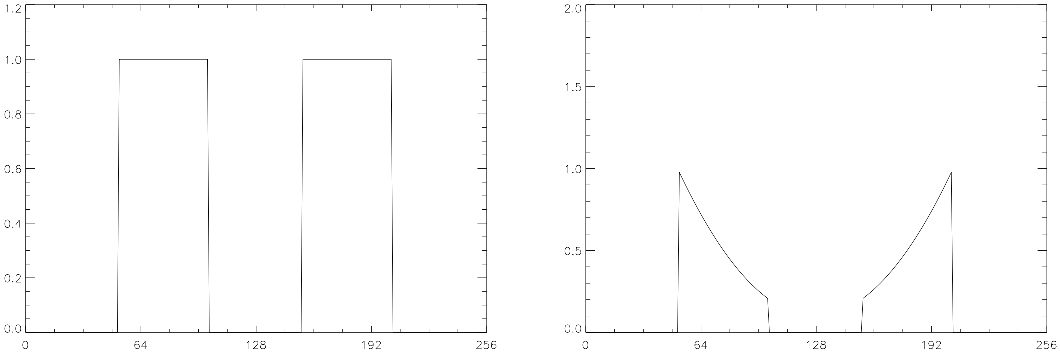

Figure 4: A 1D model problem with m on the left and r on the right, where r is the restriction to the data support of a quadratic function.

Thus, consider minimizing the following instead of (2.6):

$$J(c) = \int_\Omega |cm - r|^2 d\boldsymbol{x} + \mu \int_\Omega |D^2 c|^2 d\boldsymbol{x} \tag{2.8}$$

where $D^2 c$ is the Hessian matrix and $|D^2 c|^2$ is the sum of its squared components. The necessary optimality conditions for the minimization of (2.8) are [20]:

$$\left\{ \begin{array}{ll} \mu\Delta^2 c + m^2 c = mr, & \Omega \\ \\ \dfrac{\partial}{\partial n}\nabla c = \dfrac{\partial}{\partial n}\Delta c = 0, & \partial\Omega. \end{array} \right. \tag{2.9}$$

Figure 6 shows an estimation obtained by (2.7) ($\mu_1 \ll \mu_2$) compared to that obtained by (2.9). The latter estimation is conspicuously linear at the boundary while the former has a vanishing normal derivative. This boundary behavior is clearly understood from the boundary conditions in (2.7) and (2.9) which support constant functions and linear functions respectively. In order to permit higher growth or decay rates, the progression can be continued to higher order by penalizing $|D^\nu c|^2$ as shown in (2.3).

The ideal estimation would be independent of the proximity of $\partial\Omega$ to the data support Ω_{d}. This independence can be achieved in some sense if $\partial\Omega$ is always sufficiently distant from Ω_{d}. Because of the highly profitable option to factor the biharmonic in (2.7) with the Laplacian, consider further the case that $\mu_2 \gg \mu_1$, but suppose now that the estimate is determined on an expanded domain and then restricted to the original domain. Unfortunately, as seen in Fig. 7, the flattening effect of the vanishing normal derivative on the expanded domain can still be seen in the restriction to the original domain. The expansion and restriction procedure can also be used with (2.3) but, as discussed in Section 4, factorization is not an option and alternative efficient numerical methods must first be developed.

To avoid the dependence on the proximity of $\partial\Omega$ to Ω_{d} on a fixed Ω, consider minimizing the following variant of (2.4):

$$J(c) = \int_\Omega |cm - r|^2 d\boldsymbol{x} + \int_\Omega w|\Delta c|^2 d\boldsymbol{x} \tag{2.10}$$

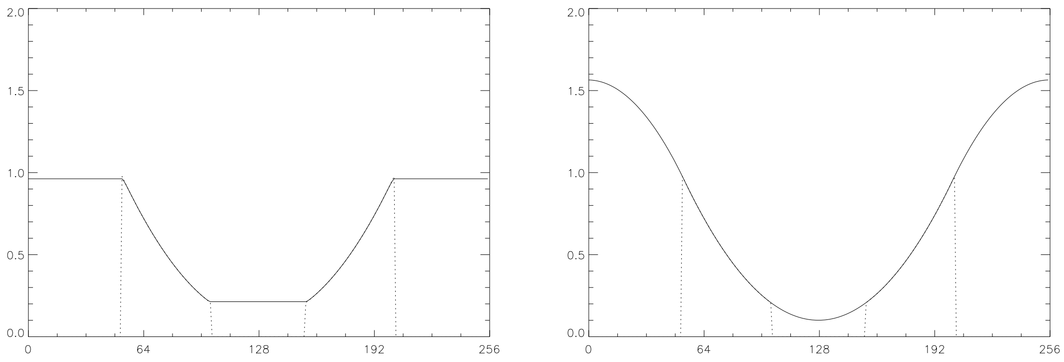

Figure 5: Estimation of c from the data in Fig. 4 using the approach of (2.7) with $\mu_1 \gg \mu_2$ on the left and $\mu_1 \ll \mu_2$ on the right.

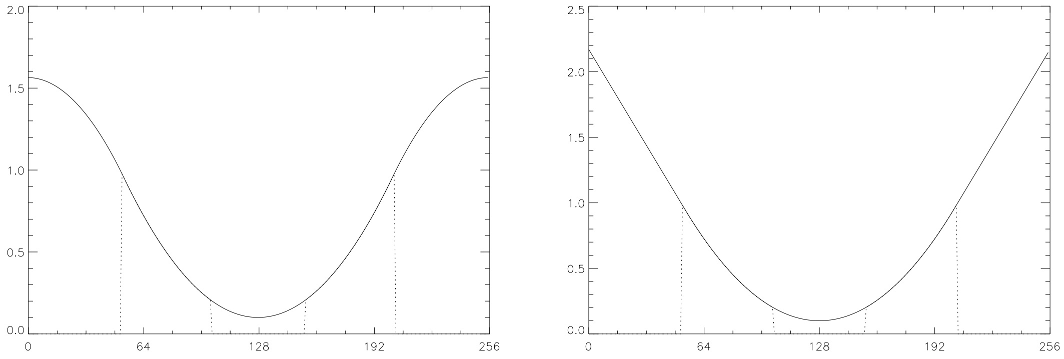

Figure 6: Estimation of c from the data in Fig. 4 using the approach of (2.7) ($\mu_1 \ll \mu_2$) shown on the left and the approach of (2.9) shown on the right.

where w is a smooth function satisfying $w > 0$ in Ω and $w \approx 0$ on $\partial\Omega$. The intent is to phase out the artificial effect of the domain outside the data support. However, the condition that $w \geq \varepsilon$ on the closure $\bar{\Omega}$ for some $\varepsilon > 0$ is necessary for the ellipticity of the optimality system. Numerical results with this approach are unstable and dependent on the value of ε and on the shape of w.

The final variant of (2.4) considered follows the work of [15]:

$$J(c) = \int_\Omega |cm - r|^2 d\boldsymbol{x} + \mu \int_\Omega |\Delta c| d\boldsymbol{x} \tag{2.11}$$

in which the function $\phi(s) = \sqrt{s}$ is proposed to afford a more local estimation in relation to the global oscillations typical of smooth spline interpolants [2]. However, for coil sensitivity estimation, the added complexity of (2.11) was not found to offer significant differences in relation to the results obtained with (2.3).

In summary, none of the penalties discussed here was found to perform better than $|D^\nu c|^2$. Furthermore, boundary conditions alternative to the natural ones will only place additional constraints on an estimate. Thus, the variational formulation adopted for this work is finally as given in (2.3). In this form, the problem is related to the surface estimation problem of early vision [14].

3 Analysis of Variational Formulation

In this section, the relevant analysis of the optimality system for (2.3), of continuous dependence on data, and of convergence in the limit of diminishing measurement error is summarized.

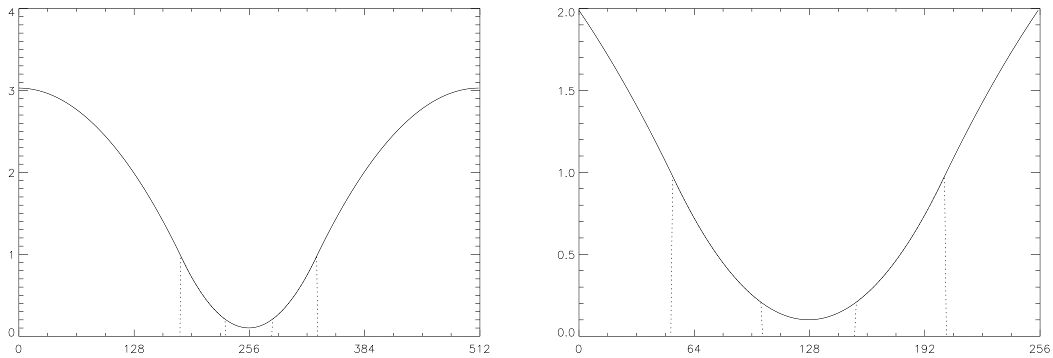

Figure 7: Estimation of c from the data in Fig. 4 using the approach of (2.7) ($\mu_1 \ll \mu_2$) on an expanded domain to the left with the result truncated to the original domain on the right.

The claims can be established using the techniques found in [11], and the details are given explicitly in [13]. For this, standard function spaces are used [1]. Specifically, $L^2(\Omega)$ denotes the space of Lebesgue measurable functions which are square integrable on Ω, and $H^\nu(\Omega)$ represents the Sobolev space of functions with distributional derivatives up to order ν in $L^2(\Omega)$. Also, the space of essentially bounded Lebesgue measurable functions is denoted by $L^\infty(\Omega)$. Here, the norms $\|\cdot\|$, semi-norms $|\cdot|$, and inner products $(\cdot,\cdot)$ are defined by:

$$\begin{array}{rclrcl}
\|c\|^2_{L^2(\Omega)} & = & \displaystyle\int_\Omega |c(\boldsymbol{x})|^2 d\boldsymbol{x} & \|c\|^2_{H^\nu(\Omega)} & = & \displaystyle\sum_{|\alpha|\le\nu} \frac{\nu!}{\alpha!}\int_\Omega |D^\alpha c(\boldsymbol{x})|^2 d\boldsymbol{x} \\
\|c\|_{L^\infty(\Omega)} & = & \displaystyle\operatorname*{ess\,sup}_{\boldsymbol{x}\in\Omega} |c(\boldsymbol{x})| & |c|^2_{H^\nu(\Omega)} & = & \displaystyle\sum_{|\alpha|=\nu} \frac{\nu!}{\alpha!}\int_\Omega |D^\alpha c(\boldsymbol{x})|^2 d\boldsymbol{x} \\
(c,h)_{L^2(\Omega)} & = & \displaystyle\int_\Omega c(\boldsymbol{x})h(\boldsymbol{x}) d\boldsymbol{x} & \langle c,h\rangle_{H^\nu(\Omega)} & = & \displaystyle\sum_{|\alpha|=\nu} \frac{\nu!}{\alpha!}\int_\Omega D^\alpha c(\boldsymbol{x}) D^\alpha h(\boldsymbol{x}) d\boldsymbol{x}.
\end{array} \tag{3.1}$$

For a fixed regularization parameter, the existence and uniqueness of a minimizer for (2.3) is given as follows.

Theorem 3.1 *Let $r \in L^2(\Omega)$ and $m \in L^\infty(\Omega)$ with $m \ge \bar{m} > 0$ on some regular domain $S \subset \Omega$. Then J in (2.3) has a unique minimizer $c \in H^\nu(\Omega)$.*

With the regularization parameter still fixed, the continuous dependence of the minimizer on the data is given as follows.

Theorem 3.2 *Assume that $\{m_n\} \subset L^\infty(\Omega)$ and $\{r_n\} \subset L^2(\Omega)$ are data for which:*

$$\lim_{n\to\infty} \|m_n - m_0\|_{L^\infty(\Omega)} = 0 \qquad \text{and} \qquad \lim_{n\to\infty} \|r_n - r_0\|_{L^2(\Omega)} = 0 \tag{3.2}$$

and $m_n \ge \bar{m} > 0$ for all n on some regular domain $S \subset \Omega$. Also, for each n let $c_n \in H^\nu(\Omega)$ denote the minimizer for J in (2.3) corresponding to data (m_n, r_n). Then:

$$\lim_{n\to\infty} \|c_n - c_0\|_{L^2(\Omega)} = 0. \tag{3.3}$$

Now convergence of minimizers in the limit of increasing data fidelity and vanishing regularization is given as follows.

Theorem 3.3 *For data $r^* \in L^2(\Omega)$ and $m^* \in L^\infty(\Omega)$ with $m^* \ge \bar{m} > 0$ on Ω, let $c^* = r^*/m^* \in H^\nu(\Omega)$. Assume that $\{m_n\} \subset L^\infty(\Omega)$ and $\{r_n\} \subset L^2(\Omega)$ are data for which:*

$$\lim_{n\to\infty} \|m_n - m^*\|_{L^\infty(\Omega)} = 0 \qquad \text{and} \qquad \lim_{n\to\infty} \|r_n - r^*\|_{L^2(\Omega)} = 0 \tag{3.4}$$

and $m_n \geq \bar{m}$ *for all* n *on some regular domain* $S \subset \Omega$*. Also, for each* n *let* $c_n \in H^\nu(\Omega)$ *denote the minimizer of* J *in (2.3) corresponding to data* (m_n, r_n) *and to regularization parameter* μ_n*. If* $\mu_n \to 0$ *at a rate for which* $\|m_n c^* - r_n\|^2_{L^2(\Omega)}/\mu_n$ *remains bounded, then:*

$$\lim_{n\to\infty} \|c_n - c^*\|_{L^2(\Omega)} = 0. \tag{3.5}$$

The condition in Theorem 3.3 that m^* have full support on Ω is somewhat unsatisfactory since this condition will never be realized in practice. Yet practitioners still speak of *the* coil sensitivity, even when it is apparently defined only by incomplete data. This intuition can be partly justified on the basis of the view that the magnetic fields in the absence of sources are *analytic* and are thus uniquely determined in Ω by their values in a regular subdomain $S \subset \Omega$. However, since the body tissue itself presents magnetic sources, the suggested analyticity is not easily justified. Even in case the data are supported only on a regular subdomain $S \subset \Omega$ and r^*/m^* has a unique analytic continuation to Ω, the data convergence stated in Theorem 3.3 is insufficient to guarantee that a limit of $\{c_n\}$ is analytic and therefore equal to c^*. However, this data convergence is all that could be expected in practice, and therefore only the solution convergence of Theorem 3.3 is considered here. The result represents at least a minimum condition that must be met by a consistent estimation method.

Now consider the characterization of a minimizer for J through its optimality system. This system will subsequently be discretized numerically to compute coil sensitivities. For $c \in H^\nu(\Omega)$, a straightforward calculation shows that the variational derivative of J is given by [20]:

$$\frac{1}{2}\frac{\delta J}{\delta c}(c; h) = B(c, h) - F(h) \tag{3.6}$$

where:

$$B(c, h) = (m^2 c, h)_{L^2(\Omega)} + \mu\langle c, h\rangle_{H^\nu(\Omega)} \tag{3.7}$$

and:

$$F(h) = (rm, h)_{L^2(\Omega)}. \tag{3.8}$$

The weak formulation of the necessary optimality condition on the minimizer $c \in H^\nu(\Omega)$ that (3.6) vanish for all $h \in H^\nu(\Omega)$ is:

$$B(c, h) = F(h) \qquad \forall h \in H^\nu(\Omega). \tag{3.9}$$

The solution is characterized as follows.

Theorem 3.4 *Let* $r \in L^2(\Omega)$ *and* $m \in L^\infty(\Omega)$ *with* $m \geq \bar{m} > 0$ *on some regular domain* $S \subset \Omega$*. Then there exists a unique* $c \in H^\nu(\Omega)$ *satisfying (3.9).*

4 Numerical Investigation

In this section, a finite difference analysis of the optimality system in (3.9) is carried out. Although high order operators are often approximated numerically with a product of low order factors, such factorizations are shown here to lead to conspicuously spurious boundary conditions for surface estimation with sparse data support. Convenient alternatives to factorization are formulated and analyzed, but it is finally proposed to use a finite element discretization investigated in Section 5.

The discretization of (3.9) begins as follows. Let Ω be divided into a grid of 2^{Np} cells, each having unit aspect ratio and width h. Specifically, with the integer component N-dimensional multi-indices $\kappa = (i, j, k, \dots)$, $\mathbf{0} = (0, 0, \dots, 0)$, and $\mathbf{1} = (1, 1, \dots, 1)$, define the cell corners by $\boldsymbol{x}_{\kappa+\frac{1}{2}} = \kappa h$, $\mathbf{0} \leq \kappa \leq 2^p \cdot \mathbf{1}$, and the cell centroids by $\boldsymbol{x}_\kappa = (\kappa - \frac{1}{2})h$, $\mathbf{1} \leq \kappa \leq 2^p \cdot \mathbf{1}$. Then, the notation C_κ is used for an approximation to $c(\boldsymbol{x}_\kappa)$, and the vector of cell values is denoted by

$\bar{C} = \{C_\kappa\}$. Also, let M denote the diagonal matrix with the squared cell values $\{m(\boldsymbol{x}_\kappa)^2\}$ on the diagonal, and let $\bar{R}$ denote the vector of cell values $\{m(\boldsymbol{x}_\kappa)r(\boldsymbol{x}_\kappa)\}$.

For simplicity, consider first the case that $N = 2$ and $\nu = 2$, for which the strong optimality system for (2.3) is written in (2.9). Now consider what has become a standard approximation of the biharmonic in terms of the square of the Laplacian; see, e.g., [14]. Specifically, with:

$$\begin{aligned} -\Delta c(\boldsymbol{x}_{ij}) \approx (L_h \bar{C})_{ij} &= h^{-2} \sum_{|k|,|l| \le 1} \ell_{i,j,k,l} C_{i+k,j+l}, && (4.1) \\ \Delta^2 c(\boldsymbol{x}_{ij}) \approx (L_h^2 \bar{C})_{ij} &= h^{-4} \sum_{|k|,|l| \le 2} b_{i,j,k,l} C_{i+k,j+l} && (4.2) \end{aligned}$$

the stencils $\{\ell_{i,j,k,l}\}$ and $\{b_{i,j,k,l}\}$ can be viewed in tabular form for field cells as follows:

$$h^2 L_h : \quad \begin{array}{ccc} & -1 & \\ -1 & 4 & -1 \\ & -1 & \end{array} \qquad h^4 L_h^2 : \quad \begin{array}{ccccc} & & 1 & & \\ & 2 & -8 & 2 & \\ 1 & -8 & 20 & -8 & 1 \\ & 2 & -8 & 2 & \\ & & 1 & & \end{array} \tag{4.3}$$

The array values shown here multiply vector elements $\{C_{i+k,j+l}\}$ where the centermost values correspond to $k = 0 = l$ and otherwise the corresponding k increases in columns from left to right while the corresponding l increases in rows from bottom to top. For the discretization of (2.7) with $\mu_1 = 0$ and $\mu_2 = \mu$,

$$[\mu_2 L_h^2 + \mu_1 L_h + M]\bar{C} = [\mu L_h^2 + M]\bar{C} = \bar{R} \tag{4.4}$$

L_h is defined in the field by the leftmost stencil in (4.3) and at the boundary, for instance at $C_{1,j}$, by subtracting the normal derivative stencil $[-1\ 1\ 0]$ from the middle row $[-1\ 4\ -1]$ to obtain $[0\ 3\ -1]$ which leaves the stencil supported in Ω. Instead of $[-1\ 1\ 0]$, the second order derivative stencil $[-1\ 2\ -1]$ can be subtracted from rows and columns of the leftmost stencil in (4.3) to eliminate stencil weights outside Ω, but this results in vanishing corner stencils and thus ambiguous corner values. So as in the continuum, the discrete Laplacian L_h necessarily involves boundary conditions of at most first order. Since the factorization $\Delta^2 \approx L_h^2$ must include those same boundary conditions, no such factorization of the biharmonic can provide a discretization of boundary conditions which are at least second order.

On the other hand, the stencil shown rightmost in (4.3) for L_h^2 at a field cell can be modified directly for cells near the boundary as illustrated by the following stencils for the cells with centroids $\{\boldsymbol{x}_{ij} : 1 \le i \le 3,\ 3 \le j \le 2^p - 2\}$:

$$\begin{array}{ccccc} & & 1 & & \\ & 0 & -4 & 1 & \\ 0 & 0 & 7 & -4 & 1 \\ & 0 & -4 & 1 & \\ & & 1 & & \end{array} \qquad \begin{array}{ccccc} & & 1 & & \\ & 1 & -8 & 2 & \\ 0 & -4 & 19 & -8 & 1 \\ & 1 & -8 & 2 & \\ & & 1 & & \end{array} \qquad \begin{array}{ccccc} & & 1 & & \\ & 2 & -8 & 2 & \\ 1 & -8 & 20 & -8 & 1 \\ & 2 & -8 & 2 & \\ & & 1 & & \end{array} \tag{4.5}$$

Here, vertical and horizontal second order derivative stencils $[-1\ 2\ -1]$ have been subtracted from the field stencil to leave all stencils supported in Ω. Other boundary stencils follow a similar pattern and are determined by the symmetry constraint, that neighboring stencil weights are reciprocal, and by the constraint that neighbors two cells away have unit weights. After dividing such stencils by h^4, let the corresponding discrete biharmonic be denoted by $\hat{B}_h$ to obtain the following discretization of the differential equation in (2.9):

$$[\mu \hat{B}_h + M]\bar{C} = \bar{R}. \tag{4.6}$$

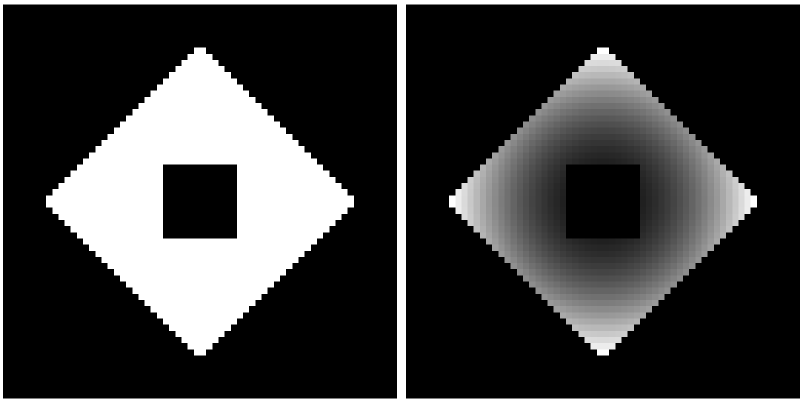

Figure 8: A 2D model problem with m on the left and r on the right, where r is is the restriction to the data support of a radially symmetric quadratic function.

This system was solved for the 2D model problem shown in figure 8, and the resulting estimation is shown in Fig. 9. Here, $m = \chi_\mathrm{d}$ where χ_d is the characteristic function for the data support Ω_d, and $r = \chi_\mathrm{d} c^*$ for a radially symmetric quadratic function c^*. Note in Fig. 9 that the left-most estimation exhibits a conspicuous departure from radial symmetry. Thus, no symmetric modification of the factorization L_h^2 was found adequate. To mend this deficiency, experimentation was performed with difference stencils to reveal that stencils having more radial symmetry better support radial symmetry in the estimation.

Specifically, consider first the purely horizontal fourth order derivative stencil $[1\ {-4}\ 6\ {-4}\ 1]$, which can be modified easily near the boundary by subtracting the second order derivative stencil $[-1\ 2\ {-1}]$ repeatedly to obtain, for instance at $C_{2,j}$ and $C_{1,j}$, the stencils $[0\ {-2}\ 5\ {-4}\ 1]$ and $[0\ 0\ 1\ {-2}\ 1]$, respectively, supported in Ω. Let the resulting 1D stencil be superimposed horizontally, vertically, and diagonally, and after dividing all resulting 2D stencils by h^4, let the corresponding difference operator be denoted by $\tilde{B}_h$. Now Fig. 9 shows an estimation obtained by solving the system:

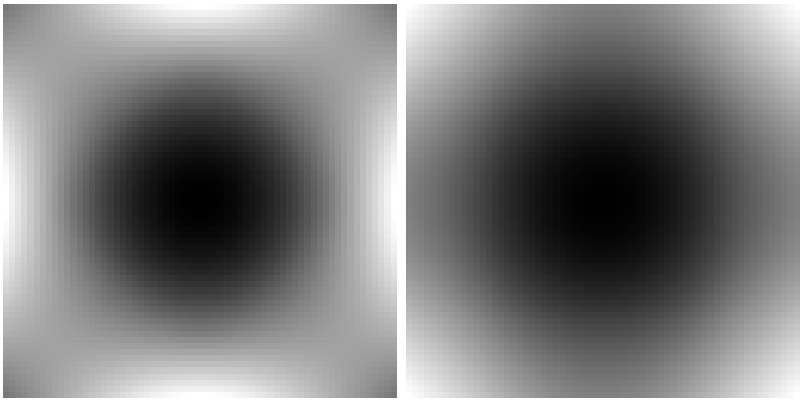

Figure 9: Estimation of c from the data in Fig. 8 using the approach of (4.6) shown on the left and the approach of (4.7) shown on the right.

$$[\mu \tilde{B}_h + M]\bar{C} = \bar{R} \tag{4.7}$$

using the same data as shown in Fig. 8. Clearly the estimation obtained using $\tilde{B}_h$ manifests better radial symmetry than that obtained using $\hat{B}_h$.

Also, higher order discretizations are readily constructed using the superposition of 1D discretizations as was done for $\tilde{B}_h$. Specifically, let the sixth and eighth order derivative stencils $[-1\ 6\ {-15}\ 20\ {-15}\ 6\ {-1}]$ and $[1\ {-8}\ 28\ {-56}\ 70\ {-56}\ 28\ {-8}\ 1]$ with their respective natural boundary conditions be superimposed horizontally, vertically, and diagonally. After dividing the resulting 2D stencils by h^6 and h^8 respectively, let these discrete operators be denoted by $\tilde{T}_h$ and $\tilde{Q}_h$. The discretizations $\tilde{B}_h$, $\tilde{T}_h$, and $\tilde{Q}_h$ were applied to the 2D model problem shown in Fig. 10, and the resulting estimations are shown in Fig. 11. Here, $m = \chi_{\rm d}$ where $\chi_{\rm d}$ is the characteristic function for the data support $\Omega_{\rm d}$, and $r = \chi_{\rm d} c^*$ for a radially symmetric quartic function c^*. Note that as a quartic function, c^* is not in the null space of any of the discrete differential operators and thus cannot provide an exact solution through the otherwise resulting equation $m^2 c^* = mr$. From the horizontal profiles shown in Fig. 11, it can be seen readily that $\tilde{Q}_h$ captures the quartic growth better than $\tilde{T}_h$ which captures quartic growth better than $\tilde{B}_h$. Also, the progressive failings in $\tilde{T}_h$ and $\tilde{B}_h$ to capture the high growth rate can be seen in the progressive departures from radial symmetry near the boundary in the corresponding images.

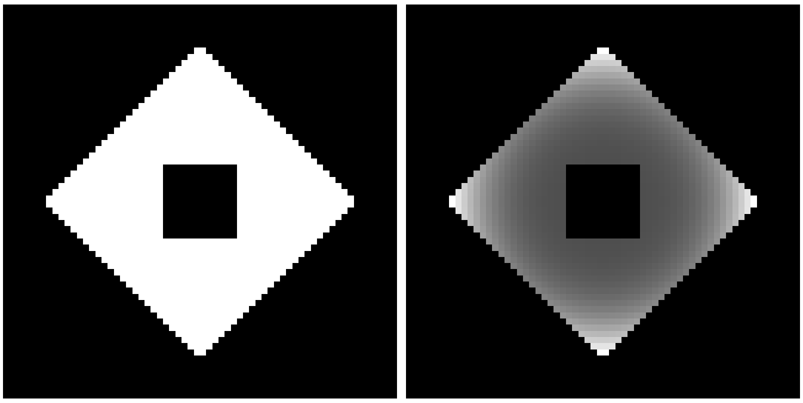

Figure 10: A 2D model problem with m on the left and r on the right, where r is the restriction to the data support of a radially symmetric quartic function.

Although these superposition difference operators, $\tilde{B}_h$, $\tilde{T}_h$, $\tilde{Q}_h$, etc., are simple to construct and provide satisfactory results, it should be emphasized that they are in fact not consistent with the original variational formulation. For instance, Taylor series expansions reveal the following for field cells in Ω:

$$\begin{aligned}
\tilde{B}_h \bar{C} &\approx 3[\partial_x^4 c + 4\partial_x^2 \partial_y^2 c + \partial_y^4 c] + \mathcal{O}(h^2) \\
\tilde{T}_h \bar{C} &\approx -3[\partial_x^6 c + 10\partial_x^4 \partial_y^2 c + 10\partial_x^2 \partial_y^4 c + \partial_y^6 c] + \mathcal{O}(h^2) \\
\tilde{Q}_h \bar{C} &\approx [3\partial_x^8 c + 56\partial_x^6 \partial_y^2 c + 140\partial_x^4 \partial_y^4 c + 56\partial_x^2 \partial_y^6 c + 3\partial_y^8 c] + \mathcal{O}(h^2).
\end{aligned} \tag{4.8}$$

Although $\hat{B}_h$ accurately approximates the biharmonic operator at field cells within $\mathcal{O}(h^2)$, all discrete differential operators introduced thus far are inconsistent with the natural boundary conditions corresponding to the variational formulation in (3.9). For instance, with ∂_n and ∂_τ denoting the boundary normal and tangential partial derivatives, respectively, the following hold at one cell off the boundary:

$$\begin{aligned}
\hat{B}_h \bar{C} &\approx (-\partial_\tau^2 c - \partial_n^2 c)h^{-2} + (\partial_n \partial_\tau^2 c + \partial_n^3 c)h^{-1} + \mathcal{O}(1) \\
\tilde{B}_h \bar{C} &\approx (-2\partial_\tau^2 c - 3\partial_n^2 c)h^{-2} + (6\partial_n \partial_\tau^2 c + 3\partial_n^3 c)h^{-1} + \mathcal{O}(1)
\end{aligned} \tag{4.9}$$

and the following hold at a cell on the boundary:

$$\begin{aligned}
\hat{B}_h \bar{C} &\approx (\partial_\tau^2 c + \partial_n^2 c)h^{-2} + (\partial_n \partial_\tau^2 c + \partial_n^3 c)h^{-1} + \mathcal{O}(1) \\
\tilde{B}_h \bar{C} &\approx (2\partial_\tau^2 c + 3\partial_n^2 c)h^{-2} + (6\partial_n \partial_\tau^2 c + 3\partial_n^3 c)h^{-1} + \mathcal{O}(1)
\end{aligned} \tag{4.10}$$

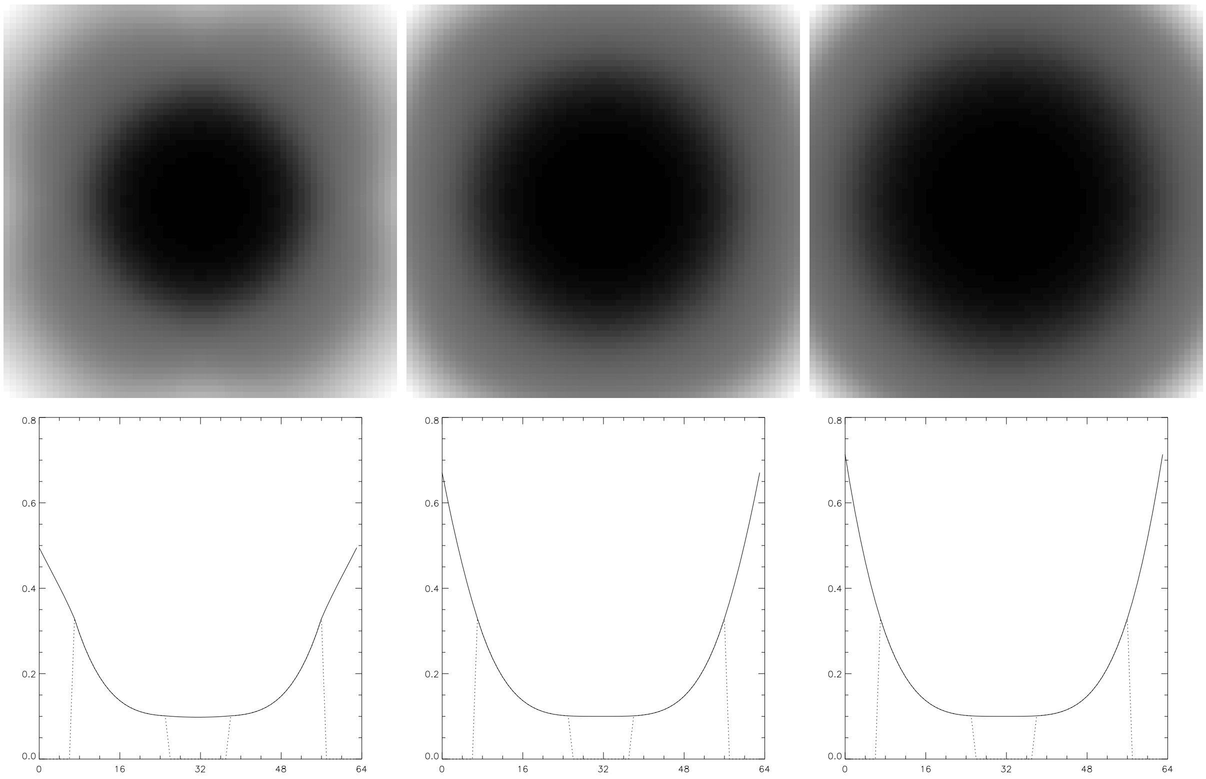

Figure 11: With the data given in Fig. 10, estimations obtained from $\tilde{B}_h$, $\tilde{T}_h$, and $\tilde{Q}_h$ are shown, respectively, in the left, middle, and right columns. The image profiles in the bottom row are taken from horizontal lines through the center of the images in the top row. Note that the lower half of the image grey-value range is rescaled for clarity.

Thus, the corresponding boundary conditions are:

$$\begin{aligned} \hat{B}_h: &\qquad \Delta c = 0, \quad \partial_n \Delta c = 0, \\ \tilde{B}_h: &\qquad \Delta c + \partial_n^2 c = 0, \quad \partial_n \partial_\tau^2 c = 0, \quad \partial_n^3 c = 0. \end{aligned} \tag{4.11}$$

Note that all harmonic functions are in the null space of $\hat{B}_h$ and not in the null space of $\tilde{B}_h$, and the superior performance of $\tilde{B}_h$ can be understood on this basis. Nevertheless, all these difference operators are distinct from the original formulation in (2.3) and (3.9), and while this distinction does not imply that the finite difference constructions are necessarily wanting, a consistent discretization of the variational formulation is naturally reached through finite elements as shown below.

5 Numerical Formulation

In this section, a consistent finite element discretization of (3.9) is formulated and analyzed. While finite elements present a natural numerical approach for solving the optimality system, it is demonstrated here that lumping is required to avoid aberrant consequences in the limit of vanishing regularization corresponding to an ever improving signal-to-noise ratio.

The boundary value problem of (3.9) is consistently discretized through finite elements as follows. For the following, let $C^\nu(\Omega)$ denote the space of functions whose derivatives up to order ν are continuous in Ω, and recall the definition of $H^\nu(\Omega)$ from section 3. Then let $S_h^\nu(\Omega) \subset C^{\nu-1}(\Omega) \cap H^\nu(\Omega)$ denote the N-fold tensor products of B-splines of degree ν defined on the grid established in Section 4 [22]. Then for a finite element approximation of the solution to the variational problem in (3.9) let $C_h \in S_h^\nu(\Omega)$ be defined by:

$$B(C_h, \chi) = F(\chi), \qquad \forall \chi \in S_h^\nu(\Omega) \tag{5.1}$$

where B and F are the same forms as in (3.9). Here, since $S_h^\nu(\Omega)$ is a closed subspace of $H^\nu(\Omega)$, the coercivity and boundedness properties established in Theorem 3.4 on $H^\nu(\Omega)$ guarantee the existence and uniqueness of the solution C_h in (5.1). This finite element approximation satisfies the following convergence property even under the minimal regularity that $c \in H^\nu(\Omega)$.

Theorem 5.1 *The respective solutions c and C_h to (3.9) and (5.1) satisfy $\|c - C_h\|_{H^\nu(\Omega)} \to 0$ as $h \to 0$.*

Proof: Convergence follows from Céa's Lemma [10] and from approximation properties detailed in [3] once c is extended outside Ω with the Calderón Extension Theorem [1]; see [13]. ■

In spite of this convergence, the practical implementation of the finite element method for coil sensitivity estimation suffers ameliorable flaws which can be understood with the 1D example of Fig. 4. The scheme (5.1) with $\nu = 2$ appears as follows in 1D. The solution is a linear combination of quadratic B-splines:

$$C_h(x) = \sum_{k=1}^{2^p+2} \gamma_k s_k(x), \qquad s_k(h(x+k-3)) = \begin{cases} \frac{2}{3}x^2, & 0 \le x \le 1 \\ 1 - \frac{4}{3}(x - \frac{3}{2})^2, & 1 \le x \le 2 \\ \frac{2}{3}(x-3)^2, & 2 \le x \le 3 \end{cases} \tag{5.2}$$

which satisfies:

$$\sum_{l=1}^{2^p+2} \Big[\mu\langle s_l, s_k\rangle_\nu + (m^2 s_l, s_k)_0\Big]\gamma_l = (rm, s_k)_0, \qquad 1 \le k \le 2^p + 2. \tag{5.3}$$

Assume that r and m are constant in a given cell with values $r_k = r(x_k)$ and $m_k = m(x_k)$. Then the above equation takes the following explicit form at interior cells:

$$\begin{aligned} &\frac{\mu}{h^4}\left[\gamma_{k+2} - 4\gamma_{k+1} + 6\gamma_k - 4\gamma_{k-1} + \gamma_{k-2}\right] \\ &\quad + \frac{1}{120}\Big[\Big(m_{k+1}^2\Big)\gamma_{k+2} + \Big(13m_{k+1}^2 + 13m_k^2\Big)\gamma_{k+1} + \Big(6m_{k+1}^2 + 54m_k^2 + 6m_{k-1}^2\Big)\gamma_k \\ &\qquad\qquad + \Big(13m_k^2 + 13m_{k-1}^2\Big)\gamma_{k-1} + \Big(m_{k-1}^2\Big)\gamma_{k-2}\Big] \\ &\qquad\qquad\qquad = \frac{1}{6}\left[(rm)_{k+1} + 4(rm)_k + (rm)_{k-1}\right] \end{aligned} \tag{5.4}$$

Figure 12 shows the result of solving this system with the data of Fig. 4. Specifically, Fig. 12 shows that when μ/h^4 is very large, the estimation is naturally quite smoothed in relation to the data. To bring the estimation ever closer to the data requires that μ/h^4 be smaller, and in practice it is desirable for the method to provide consistent results in the limit that $\mu/h^4 \to 0$ as the signal-to-noise ratio becomes ever better. However, the numerical result here is quite aberrant as μ/h^4 becomes very small. This behavior can be understood readily by observing (5.4) for the case that $r = m = 1$ on the data support shown in Fig. 12. The expected constant solution nullifies the discrete differential operator, which appears multiplied by μ in (5.4). However, across data discontinuities, the constant solution does not satisfy what remains of the difference equation in (5.4). On the other hand, the following *lumped* formulation suffers no such failure in consistency even for the limiting case that $\mu/h^4 \to 0$:

$$\frac{\mu}{h^4}\left[\gamma_{k+2} - 4\gamma_{k+1} + 6\gamma_k - 4\gamma_{k-1} + \gamma_{k-2}\right] + m_k^2\gamma_k = r_k m_k. \tag{5.5}$$

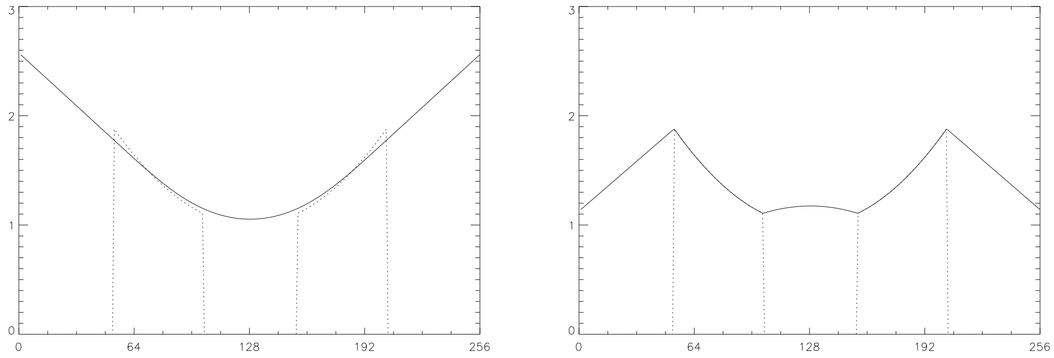

Figure 12: Solutions of the model problem in Fig. 4 using (5.4) with the case that μ/h^4 is large shown on the left, and the case that μ/h^4 is small shown on the right.

This observation suggests using the finite element formulation to provide a consistent finite differencing of the differential operator and its boundary conditions, but otherwise lumping parameters on zero-order terms.

Specifically, let $s(\boldsymbol{x})$ be the canonical B-spline function of degree ν with support in $[\mathbf{0}, \nu+\mathbf{1}]$ whose dilation and then translations, $s_\kappa(\boldsymbol{x}) = s(h^{-1}(\boldsymbol{x} - \boldsymbol{x}_{\kappa-(\nu+\frac{1}{2})}))$, $\mathbf{1} \le \kappa \le (2^p+\nu)\cdot\mathbf{1}$, provide the basis functions for $S_h^\nu(\Omega)$. Then, for $\mathbf{1} \le \kappa \le 2^p \cdot \mathbf{1}$, define the shifted spline $\sigma_\kappa(\boldsymbol{x}) = s(h^{-1}(\boldsymbol{x} - \boldsymbol{x}_{\kappa-\frac{1}{2}(\nu+1)}))$ which peaks at $\boldsymbol{x}_\kappa$. Also, let $\chi_\kappa(\boldsymbol{x})$ be the characteristic function for the cell with centroid $\boldsymbol{x}_\kappa$. Then the data and solution are represented as piecewise constant functions:

$$C_h(\boldsymbol{x}) = \sum_{\mathbf{1}\le\kappa\le 2^p\cdot\mathbf{1}} \gamma_\kappa \chi_\kappa(\boldsymbol{x}), \qquad m(\boldsymbol{x}) = \sum_{\mathbf{1}\le\kappa\le 2^p\cdot\mathbf{1}} m_\kappa \chi_\kappa(\boldsymbol{x}), \qquad r(\boldsymbol{x}) = \sum_{\mathbf{1}\le\kappa\le 2^p\cdot\mathbf{1}} r_\kappa \chi_\kappa(\boldsymbol{x}) \tag{5.6}$$

and the solution is defined by:

$$\sum_{\mathbf{1}\le\lambda\le 2^p\cdot\mathbf{1}} \left[\mu\langle\sigma_\lambda, \sigma_\kappa\rangle_{H^\nu(\Omega_\nu)} + (m^2\chi_\lambda, \chi_\kappa)_{L^2(\Omega)}\right]\gamma_\lambda = (rm, \chi_\kappa)_{L^2(\Omega)}, \qquad \mathbf{1} \le \kappa \le 2^p\cdot\mathbf{1} \tag{5.7}$$

where $\Omega_\nu = [\frac{\nu}{2}h\cdot\mathbf{1}, (2^p - \frac{\nu}{2})h\cdot\mathbf{1}]$. For comparison with the finite difference schemes detailed in the previous section, take $N = 2$ and $\nu = 2$ and let B_h denote the discrete biharmonic operator multiplying μ in (5.7), whose stencils are given explicitly as follows for the cells with centroids $\{\boldsymbol{x}_\kappa : \mathbf{1} \le \kappa \le 3\cdot\mathbf{1}\}$, where stencil weights are obtained by dividing the following by $2800h^4$:

$$\begin{array}{rrrrr}
0 & 0 & -152 & 424 & 208 \\
0 & 0 & -592 & -2176 & 848 \\
0 & 0 & 4368 & -2256 & 768 \\
0 & 0 & -592 & -2176 & 848 \\
0 & 0 & -152 & 424 & 208
\end{array}
\qquad
\begin{array}{rrrrr}
0 & 424 & 920 & 848 & 208 \\
0 & -2176 & -3920 & -4352 & 848 \\
0 & -2256 & 20400 & -4512 & 768 \\
0 & -2176 & -3920 & -4352 & 848 \\
0 & 424 & 920 & 848 & 208
\end{array}
\qquad
\begin{array}{rrrrr}
208 & 848 & 768 & 848 & 208 \\
848 & -4352 & -4512 & -4352 & 848 \\
768 & -4512 & 24768 & -4512 & 768 \\
848 & -4352 & -4512 & -4352 & 848 \\
208 & 848 & 768 & 848 & 208
\end{array}$$

$$\begin{array}{rrrrr}
0 & 0 & -152 & 424 & 208 \\
0 & 0 & -592 & -2176 & 848 \\
0 & 0 & 3440 & -1960 & 920 \\
0 & 0 & -296 & -1088 & 424 \\
0 & 0 & 0 & 0 & 0
\end{array}
\qquad
\begin{array}{rrrrr}
0 & 424 & 920 & 848 & 208 \\
0 & -2176 & -3920 & -4352 & 848 \\
0 & -1960 & 16960 & -3920 & 920 \\
0 & -1088 & -1960 & -2176 & 424 \\
0 & 0 & 0 & 0 & 0
\end{array}
\qquad
\begin{array}{rrrrr}
208 & 848 & 768 & 848 & 208 \\
848 & -4352 & -4512 & -4352 & 848 \\
920 & -3920 & 20400 & -3920 & 920 \\
424 & -2176 & -2256 & -2176 & 424 \\
0 & 0 & 0 & 0 & 0
\end{array}$$

$$\begin{array}{rrrrr}
0 & 0 & -152 & 424 & 208 \\
0 & 0 & -296 & -1088 & 424 \\
0 & 0 & 928 & -296 & -152 \\
0 & 0 & 0 & 0 & 0 \\
0 & 0 & 0 & 0 & 0
\end{array}
\qquad
\begin{array}{rrrrr}
0 & 424 & 920 & 848 & 208 \\
0 & -1088 & -1960 & -2176 & 424 \\
0 & -296 & 3440 & -592 & -152 \\
0 & 0 & 0 & 0 & 0 \\
0 & 0 & 0 & 0 & 0
\end{array}
\qquad
\begin{array}{rrrrr}
208 & 848 & 768 & 848 & 208 \\
424 & -2176 & -2256 & -2176 & 424 \\
-152 & -592 & 4368 & -592 & -152 \\
0 & 0 & 0 & 0 & 0 \\
0 & 0 & 0 & 0 & 0
\end{array}$$

Then, (5.7) is approximated as follows:

$$[\mu B_h + M]\bar{C} = \bar{R}. \tag{5.8}$$

Now consider the following consistency properties of B_h. For field cells in Ω:

$$B_h\bar{C} \quad \approx \quad [\partial_x^4 c + 2\partial_x^2\partial_y^2 c + \partial_y^4 c] + \mathcal{O}(h^2). \tag{5.9}$$

At one cell off the boundary:

$$B_h\bar{C} \;\approx\; -\partial_n^2 c h^{-2} + (\partial_n\partial_\tau^2 c + \partial_n^3 c)h^{-1} + \mathcal{O}(1). \tag{5.10}$$

At a cell on the boundary at least two cells from a corner:

$$B_h\bar{C} \;\approx\; \partial_n^2 c h^{-2} + (\partial_n\partial_\tau^2 c + \partial_n^3 c)h^{-1} + \mathcal{O}(1). \tag{5.11}$$

These two properties lead to the boundary conditions that $\partial_n^2 c = 0$ then $\partial_n^3 c = 0$ and finally $\partial_\tau\partial_n^2 c = 0$. Then, the sum of terms for the four cells at, or one cell off, a corner gives:

$$B_h\bar{C} \;\approx\; 2\partial_n\partial_\tau c h^{-2} + (\partial_\tau^3 c + 3\partial_n\partial_\tau^2 c + 3\partial_n^2\partial_\tau c + \partial_n^3 c)h^{-1} + \mathcal{O}(1). \tag{5.12}$$

Thus, the corner condition $\partial_n\partial_\tau c = 0$ combined with the condition $\partial_\tau^2\partial_n c = 0$ along the edges implies that $\partial_n\partial_\tau c$ remains zero along the edges. Therefore, the boundary conditions corresponding to the above expansions for B_h are:

$$B_h: \quad \partial_n\Delta c = 0, \quad \partial_n^2 c = 0, \quad \partial_n\partial_\tau c = 0 \tag{5.13}$$

matching those shown in (2.9).

Next, the 2D model problem shown in Fig. 13 provides a good comparison for $\tilde{B}_h$ and B_h, and their respective estimations are shown in Fig. 14. The profiles shown in Fig. 14 illustrate an improvement gained from using B_h instead of $\tilde{B}_h$.

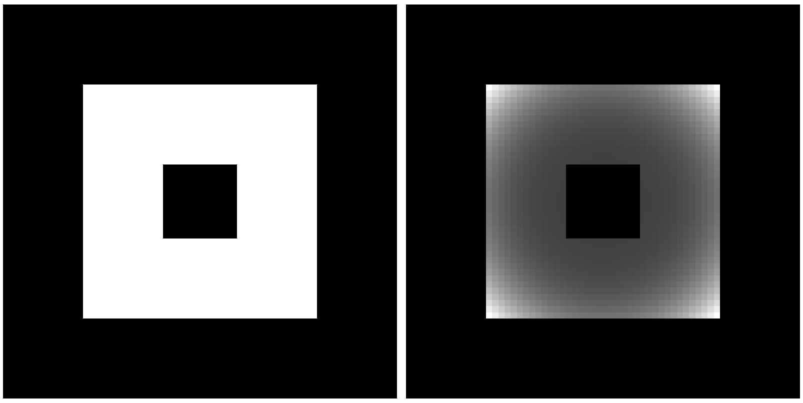

Figure 13: A 2D model problem with m on the left and r on the right, where r is the restriction to the data support of a radially symmetric quartic function.

Higher order discretizations T_h and Q_h obtained from (5.7) for $\nu = 3$ and $\nu = 4$, respectively, have also been applied to the data appearing in Fig. 13, and their estimations are shown in Figs. 15 and 16, respectively. The profiles shown in Figs. 15 and 16 also demonstrate an improvement gained from using T_h and Q_h instead of $\tilde{T}_h$ and $\tilde{Q}_h$, respectively.

Concerning the numerical procedure for solving (5.7), note first the following guarantee of solvability.

Theorem 5.2 *Suppose r and m are given by (5.6) and that there is a collection of adjacent cells in $\Omega_\nu = [\frac{\nu}{2}h \cdot \mathbf{1}, (2^p - \frac{\nu}{2})h \cdot \mathbf{1}]$ with centroids $\{\boldsymbol{x}_\kappa : \kappa_1 \le \kappa \le \kappa_1 + \nu\}$ in which $m_\kappa \ne 0$. Then the coefficient matrix in (5.7) is symmetric and positive definite.*

Proof: The matrix is evidently symmetric. Suppose there exist coefficients $\{\gamma_\kappa\}$ such that

$$\sum_{\mathbf{1}\le\kappa\le 2^p\cdot\mathbf{1}} \sum_{\mathbf{1}\le\lambda\le 2^p\cdot\mathbf{1}} \left[\mu\langle\sigma_\lambda,\sigma_\kappa\rangle_{H^\nu(\Omega_\nu)} + (m^2\chi_\lambda,\chi_\kappa)_{L^2(\Omega)}\right]\gamma_\lambda\gamma_\kappa = 0. \tag{5.14}$$

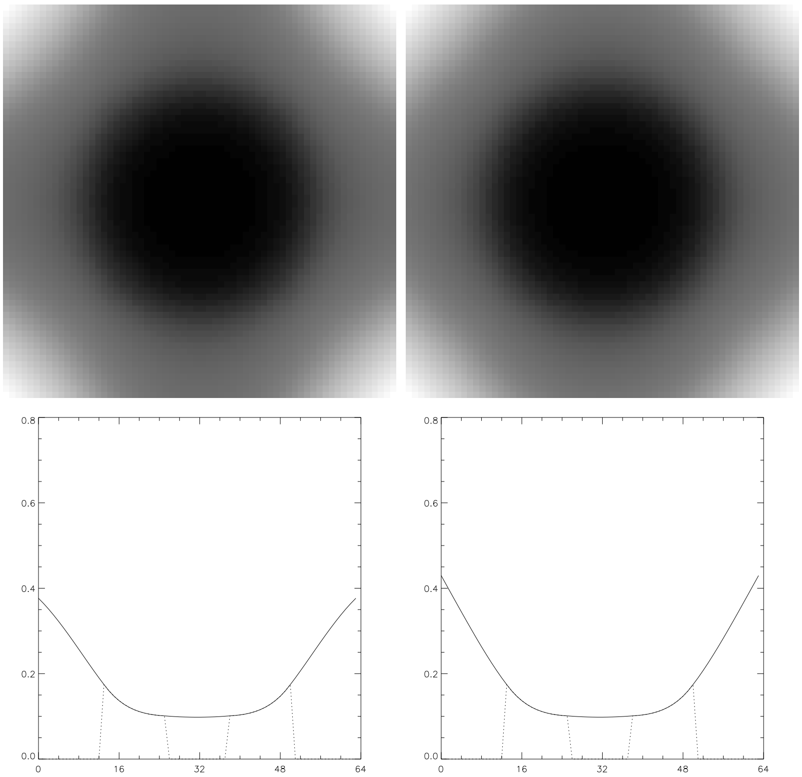

Figure 14: With the data given in Fig. 13, estimations obtained from $\tilde{B}_h$ and B_h are shown in the left and right columns, respectively. The image profiles in the bottom row are taken from horizontal lines through the center of the images in the top row. Note that the lower half of the image grey-value range is rescaled for clarity.

Then the functions:

$$f = \sum_{\mathbf{1} \le \kappa \le 2^p \cdot \mathbf{1}} \gamma_\lambda \sigma_\kappa \qquad g = \sum_{\mathbf{1} \le \lambda \le 2^p \cdot \mathbf{1}} \gamma_\lambda \chi_\lambda \tag{5.15}$$

satisfy:

$$\mu \langle f, f \rangle_{H^\nu(\Omega_\nu)} + (mg, mg)_{L^2(\Omega)} = 0 \qquad \text{or} \qquad |f|_{H^\nu(\Omega_\nu)} = \|mg\|_{L^2(\Omega)} = 0. \tag{5.16}$$

Therefore, $f \in P_{\nu-1}(\Omega_\nu) \subset P_\nu(\Omega_\nu)$ where $P_n(\Omega)$ represents the polynomials of degree at most n in Ω. Now define $\kappa_2 = \kappa_1 + \nu$, $\kappa_0 = \frac{1}{2}(\kappa_1 + \kappa_2)$, and $S = [\boldsymbol{x}_{\kappa_0 - \frac{1}{2}}, \boldsymbol{x}_{\kappa_0 + \frac{1}{2}}]$. Then notice that σ_κ is supported in S, i.e., $[\boldsymbol{x}_{\kappa_0 - \frac{1}{2}}, \boldsymbol{x}_{\kappa_0 + \frac{1}{2}}] \cap [\boldsymbol{x}_{\kappa - \frac{1}{2}(\nu+1)}, \boldsymbol{x}_{\kappa + \frac{1}{2}(\nu+1)}] \neq \emptyset$, precisely when $\kappa_1 \le \kappa \le \kappa_2$. Thus, f is given in S by:

$$f(\boldsymbol{x}) = \sum_{\kappa_1 \le \kappa \le \kappa_2} \gamma_\kappa \sigma_\kappa(\boldsymbol{x}). \tag{5.17}$$

Since the right-hand side here lies in $P_\nu(S)$, it gives the unique analytic continuation of f from $P_\nu(S)$ to $P_\nu(\Omega_\nu)$. As $\|mg\|_{L^2(\Omega)} = 0$ and $m_\kappa \neq 0$ for $\kappa_1 \le \kappa \le \kappa_2$, it follows that $g(\boldsymbol{x}_\kappa) = \gamma_\kappa = 0$ for $\kappa_1 \le \kappa \le \kappa_2$ and therefore $f = 0 = g$. ■

According to this theorem, the system in (5.7) can be solved using the conjugate gradient method. In fact, conjugate gradient has been used to solve all linear systems presented in this paper. Also, the preconditioning obtained with hierarchical basis conjugate gradient [23] has been investigated for this work, and its success has been found to depend heavily on the matching between the local scales represented in the hierarchical basis and the local scales present in the data. The preferred solution procedure for (5.7) involves multigrid techniques [24], and further numerical details will be reported separately.

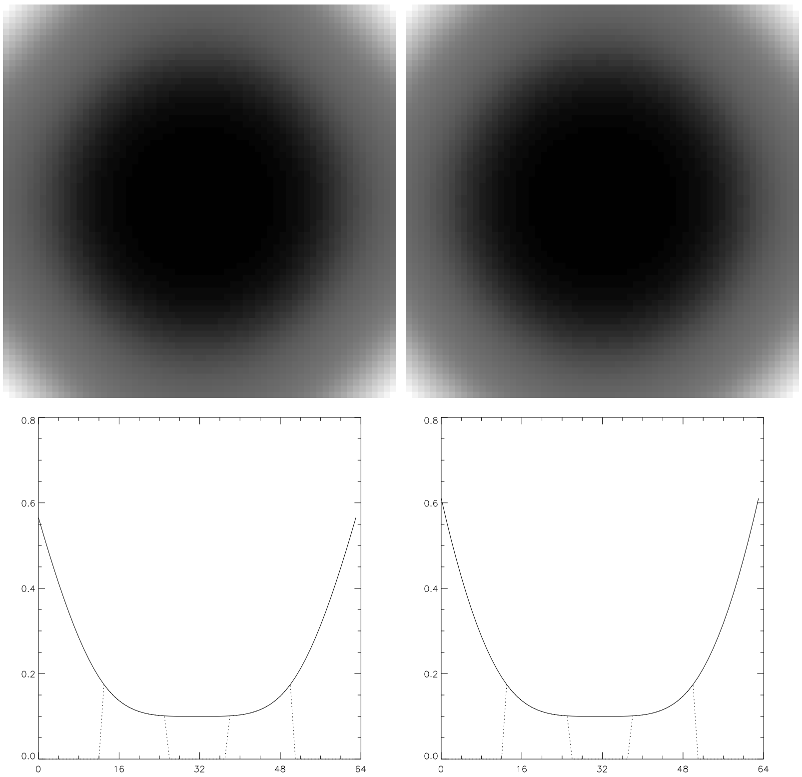

Figure 15: With the data given in Fig. 13, estimations obtained from $\tilde{T}_h$ and T_h are shown in the left and right columns, respectively. The image profiles in the bottom row are taken from horizontal lines through the center of the images in the top row. Note that the lower half of the image grey-value range is rescaled for clarity.

6 Applications

In this section, the accuracy of the proposed coil sensitivity estimation procedure is illustrated in terms of realistic examples. In particular, magnetic resonance images of phantoms are used to demonstrate the importance of accurate sensitivity estimation for SENSE image reconstruction, and the proposed approach is shown to perform quite well.

First, Fig. 2 shows the magnitude plots $|\mathcal{U}_{\mathrm{b}}|$ and $|\mathcal{U}_{\mathrm{s}}|$ for body coil and surface coil images respectively. The figure also shows the magnitude plot $|\mathcal{C}|$ of a coil sensitivity estimation obtained using the two residual equations in (2.1) for $\Re(\mathcal{C})$ and $\Im(\mathcal{C})$ and solving (5.7) with $\nu = 4$. Since in this case the optimality system for (2.3) involves homogeneous boundary conditions of order not smaller than $\nu = 4$, cubic polynomial growth at the boundary is supported. The choice of regularization parameter μ was made manually by seeking a smooth fit to the data on their support while avoiding oscillations and over-smoothing, particularly at the edge of the data support. Automatic methods for determining μ involve relating a known signal-to-noise ratio to the residual term in J and then solving for an appropriate regularization parameter [21]; however, such methods are not pursued in the present work.

To address the accuracy of estimation in terms of a simpler example, consider the 1D estimation in Fig. 17. Here the desired cubic solution c^* is plotted with a dotted line. On the support of the solid curve, $m = 1$ and otherwise $m = 0$. The solid curve is r, given by the noise corrupted product mc^*. The dashed curve on the left is an estimation c_1 of c^* obtained by solving (4.4), and the dashed curve on the right is an estimation c_2 of c^* obtained by solving (5.7) with $\nu = 4$. Note in particular that the dashed curve on the left provides an especially poor estimation of c^* at the leftmost data support edge, while the estimation on the right is quite good. The profiles from the real and imaginary parts associated with the images in Fig. 2 exhibit the same behavior seen on the right in Fig. 17.

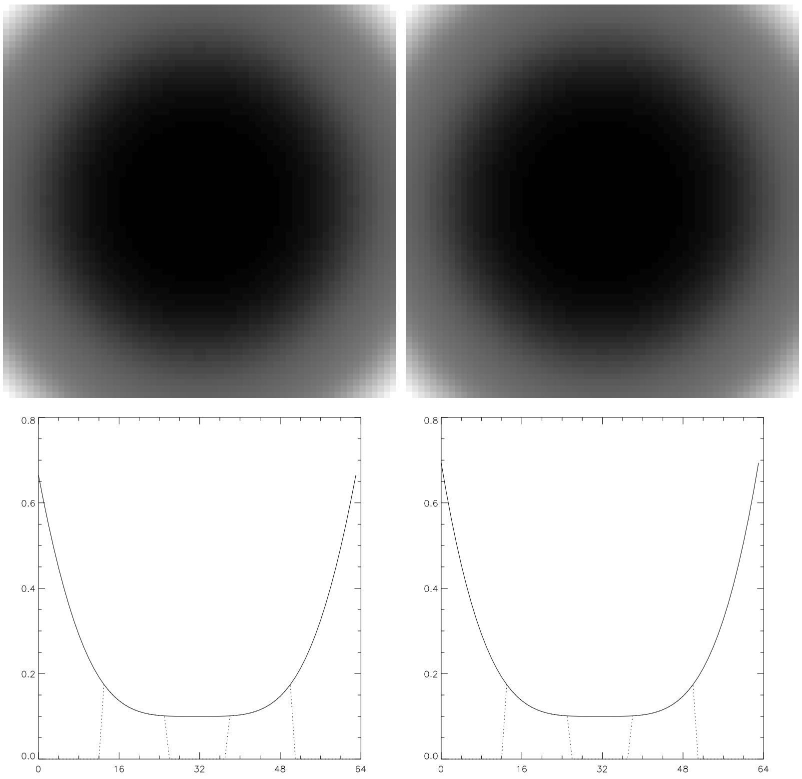

Figure 16: With the data given in Fig. 13, estimations obtained from $\tilde{Q}_h$ and Q_h are shown in the left and right columns, respectively. The image profiles in the bottom row are taken from horizontal lines through the center of the images in the top row. Note that the lower half of the image grey-value range is rescaled for clarity.

In general, the precise measure of accuracy is given here in Theorem 3.3, and involves the limit as the data support approaches full measure in Ω. Although such conditions must be met by a consistent estimation method, in practice, the data support is always a strict subset of the measurement field. To show how errors such as those seen in Fig. 17 manifest themselves in practice, the estimation procedure will now be demonstrated for SENSE image reconstruction [19]. In this application, coils operate in parallel but they undersample the available signal in order to achieve a high acquisition rate. The undersampling leads to an aliased image for each coil, but knowledge of the respective coil sensitivities can be used to reconstruct a single unaliased image. On the other hand, the reconstructed image is susceptible to ghosting artifacts resulting from inaccurate coil sensitivities. These details will now be demonstrated with magnetic resonance images of phantoms.

The four images $\{\mathcal{U}_{\mathrm{s}_i}\}_{i=1}^4$ shown in Fig. 18 are simulated surface coil images generated using the body coil image $\mathcal{U}_{\mathrm{b}}$ of the phantom shown at the left in Fig. 19. Specifically, the surface coil images were obtained by multiplying the body coil image by four separate typical coil sensitivities $\{\mathcal{C}_i\}_{i=1}^4$ and then folding the resulting images vertically over themselves twice. This folding simulates the aliasing mentioned above. Knowledge of the respective coil sensitivities can be used as follows to reconstruct an unaliased image $\mathcal{U}^*$. If Δy is the height of the folded images, then the following equations hold for each (x, y) in the domain of the surface coil images:

$$\mathcal{U}_{\mathrm{s}_i}(x, y) = \sum_{j=1}^{4} \mathcal{C}_i(x, y + j\Delta y)\mathcal{U}^*(x, y + j\Delta y), \qquad 1 \leq i \leq 4. \tag{6.1}$$

Solving these systems for each (x, y) provides the so-called SENSE reconstructed image $\mathcal{U}^*$.

Figure 19 now demonstrates the effect of the coil sensitivity estimation on the SENSE reconstruction. The data used for coil sensitivity estimation were $\mathcal{U}_{\mathrm{b}}$ and noise corrupted products $\mathcal{C}_i\mathcal{U}_{\mathrm{b}}$. The SENSE reconstructions in the middle and to the right in Fig. 19 were obtained from

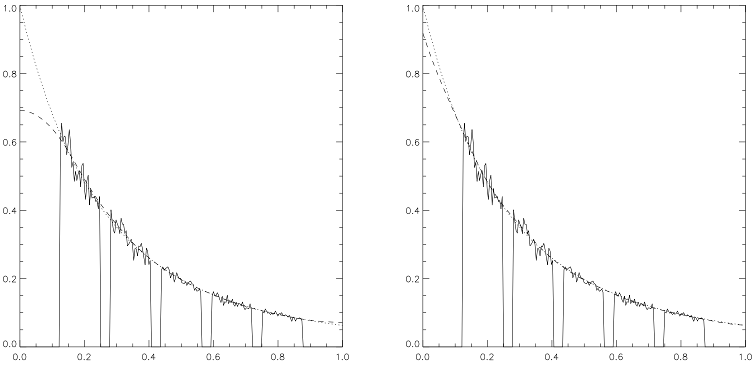

Figure 17: At the left are a noise corrupted r (solid), an exact sensitivity c^* (dotted), and a sensitivity c_1 (dashed) estimated by solving (4.4). At the right are r (solid), c^* (dotted), and a sensitivity c_2 (dashed) estimated by solving (5.7) with $\nu = 4$.

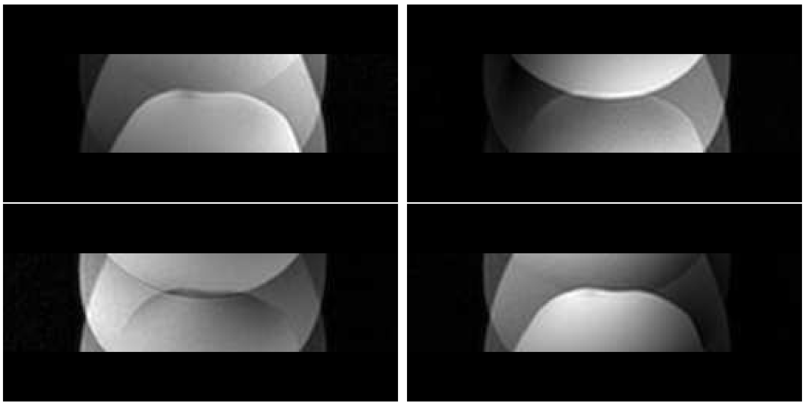

Figure 18: Aliased surface coil images $\mathcal{U}_{s_i}$, $1 \le i \le 4$.

coil sensitivities estimated, respectively, by solving (4.4) and (5.8). Note in the middle image of Fig. 19 the ghost outlines of spuriously unfolded image boundaries resulting from coil sensitivity estimation insufficiencies such as those displayed in Fig. 17. On the other hand, the image at the right in Fig. 19 suffers much less so from such ghostings, even with $\nu = 2$. The phantom image at the left in Fig. 19 was used here to demonstrate ghosting clearly, but these ghost outlines would be superimposed on genuine anatomical features in more realistic applications. Avoiding such artifacts is naturally more difficult as the signal-to-noise ratio decreases and as the patient motion between serial measurements increases. For further details of the authors' work on the applications which motivated this investigation, see [7], [8], and [9].

7 Summary

A variational approach to estimating a magnetic resonance coil sensitivity from its corresponding nonuniform illumination of magnetic resonance images has been proposed and analyzed both theoretically and computationally. In the selected procedure, the sum of a residual and a high order penalty is minimized. The residual is derived from the rough sensitivity estimate given by the quotient of images obtained with and without uniform illumination. Higher order penalties together with their natural boundary conditions capture higher sensitivity decay rates implicitly and non-parametrically. The resulting formulation parallels that of the surface estimation problem of early vision. The relevant analysis of the optimality system, of continuous dependence on data, and of convergence in the limit of diminishing measurement error has been summarized. Finite difference analysis of the optimality system has revealed that typical

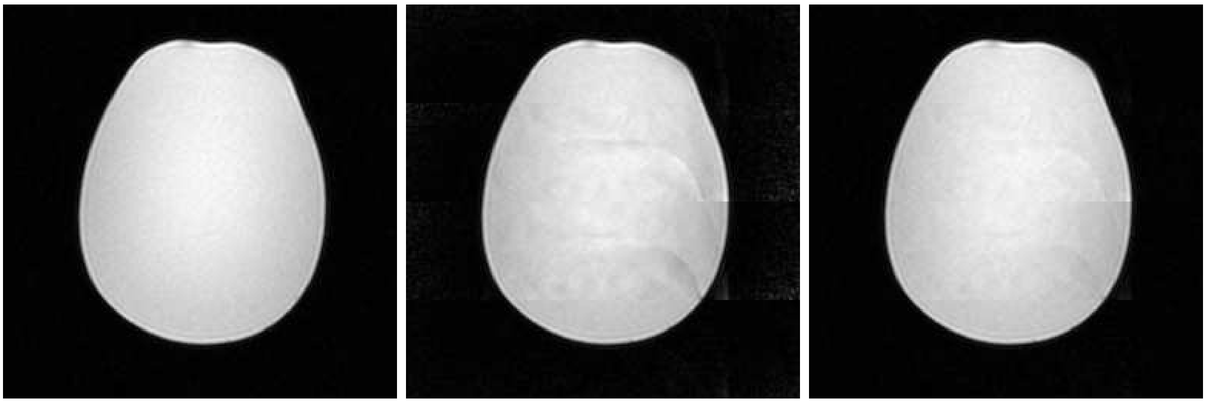

Figure 19: Shown at the left is a body coil image $\mathcal{U}_\mathrm{b}$. The images in the middle and at the right are reconstructions of $\mathcal{U}_\mathrm{b}$ from $\mathcal{U}_{\mathrm{s}_i}$ in Fig. 18, and from estimations of the sensitivities $\mathcal{C}_i$ obtained, respectively, by solving (4.4) and (5.8).

factorizations of high order operators into low order products lead to conspicuously spurious boundary conditions for surface estimation with sparse data support. As an alternative, superpositions of one-dimensional difference operators have been formulated and analyzed, but a lumped finite element discretization has been found preferable on the basis of its consistency with the optimality system and its accuracy of estimation. It has been demonstrated further that finite element lumping is required in case of discontinuous data in order to avoid aberrant consequences in the limit of vanishing regularization corresponding to an ever improving signal-to-noise ratio. To justify the selection of the proposed estimation procedure, it has been applied along with several of its alternatives to simple examples as well as measured magnetic resonance images. Finally, magnetic resonance images of phantoms have been used to demonstrate the importance of accurate sensitivity estimation for SENSE image reconstruction, and the proposed approach has been shown to perform quite well. In forthcoming work the rapid calculation of coil sensitivities with the use of multigrid techniques will be reported.

References

[1] R.A. Adams, *Sobolev Spaces*, Academic Press, New York, London, Toronto, Sydney, San Francisco, 1975.

[2] H. Akima, *A New Method of Interpolation and Smooth Curve Fitting based on Local Procedures*, J. Assoc. Comput. Mach., Vol. 17, pp. 589–602, 1970.

[3] J. Aubin, *Approximation of Elliptic Boundary-Value Problems*, Krieger, Huntington, New York, 1980.

[4] L. Axel, J. Constantini, J. Listerud, *Intensity Correction in Surface-Coil MR Imaging*, Am. J. Radiol., Vol. 148, pp. 418–420, 1987.

[5] M.A.G. Ballester, Y. Machida, Y. Kassai, Y. Hamamura, H. Sugimoto, *Robust Estimation of Coil Sensitivities for RF Subencoding Acquisition Techniques*, Annual Meeting of ISMRM, Glasgow, April 21-27, 2001.

[6] R. Bammer, R. Stollberger, M. Augustin, T. Seifert, S. Strasser-Fuchs, H.P. Hartung, and F. Fezekas, *Parallel Imaging Strategies for High-Speed Magnetic Resonance Diffusion Imaging*, SPIE International Symposium on Medical Imaging, San Diego, CA, February 12-18, 2000.

[7] R. Bammer, S.L. Keeling, M. Augustin, K.P. Pruessmann, R. Wolf, R. Stollberger, H. Hartung, F. Fazekas, *Improved Diffusion-Weighted Single-Shot Echo-Planar Imaging in Stroke using Sensitivity Encoding*, Magnetic Resonance in Medicine, Vol. 46, No. 3, pp. 548–554, September 2001.

[8] R. Bammer, S.L. Keeling, M. Auer, K.P. Pruessmann, P. Roeschmann, R. Stollberger, F. Fazekas, *Diffusion Tensor Imaging using SENSE-Single-Shot EPI*, Annual Meeting of ISMRM the International Society for Magnetic Resonance in Medicine, Glasgow, April 21-27, 2001.

[9] R. Bammer, S.L. Keeling, M. Augustin, K.P. Pruessmann, C. Leussler, F. Fazekas, *Improved Diffusion-Weighted Single-Shot EPI in Stroke using SENSE*, Annual Meeting of ISMRM the International Society for Magnetic Resonance in Medicine, Glasgow, April 21-27, 2001.

[10] P.G. Ciarlet, *The Finite Element Method for Elliptic Problems*, North-Holland, Amsterdam, New York, Oxford, 1978.

[11] H.W. Engl, M. Hanke, A. Neubauer, *Regularization of Inverse Problems*, Kluwer, Dordrecht, 1996.

[12] E.M. Haacke, R. W. Brown, M.R. Thompson, R. Venkatesan, *Magnetic Resonance Imaging: Physical Principles and Sequence Design*, John Wiley, New York, Chichester, Brisbane, Toronto, 1999.

[13] S.L. Keeling and R. Bammer, *A Variational Approach to Magnetic Resonance Coil Sensitivity Estimation*, SFB Report No. 207, Karl-Franzens-University of Graz, Graz, Austria, December 2000.

[14] S.H. Lai and B.C. Vemuri, *Physically-based Adaptive Preconditioning for Early Vision*, IEEE Transactions on Pattern Analysis and Machine Intelligence, Vol. 19, No. 6, pp. 594–607, 1997.

[15] J.E. Lavery, *Shape-Preserving, Multiscale Interpolation by Bi- and Multivariate Cubic L_1 Splines*, CAGD, Vol. 18, No. 4, pp. 321–343, 2001.

[16] Z. Liang and P.C. Lauterbur, *Principles of Magnetic Resonance Imaging: A Signal Processing Perspective*, IEEE Press, Picsataway, 2000.

[17] F. Lin, L.L. Wald, Y. Chen, J.W. Belliveau, *Estimation of Coil Sensitivity Map and Correction of Surface Coil Magnetic Resonance Images using Wavelet Decomposition*, Annual Meeting of ISMRM, Glasgow, April 21-27, 2001.

[18] W.H. Press, B.P. Flannery, S.A. Teukolsky, W.T. Vetterling, *Numerical Recipes: The Art of Scientific Computing*, Cambridge University Press, Cambridge, New York, Port Chester, Melbourne, Sydney, 1989.

[19] K.P. Pruessman, M. Weiger, M.B. Scheidegger, P. Boesiger, *SENSE: sensitivity encoding for fast MRI*, Magn. Reson. Med., Vol. 42, pp. 952–962, 1999.

[20] K. Rektorys, *Variational Methods in Mathematics, Science and Engineering*, Reidel, Dordrecht, Boston, 1977.

[21] L.I. Rudin, S. Osher, and E. Fatemi, *Nonlinear Total Variation Based Noise Removal Algorithms*, Physica D, Vol. 60, pp. 259–268, 1992.

[22] L.L. Schumaker, *Spline Functions: Basic Theory*, John Wiley, New York, Chichester, Brisbane, Toronto, 1981.

[23] R. Szeliski, *Fast Surface Interpolation Using Hierarchical Basis Functions*, IEEE Trans. Pattern Anal. Machine Intell., Vol. 12, No. 6, pp. 513–528, 1990.

[24] U. Trottenberg, C. Oosterlee, and A. Schüller, *Multigrid*, Academic Press, San diego, San Francisco, New York, Boston, London, Sydney, Tokyo, 2001.